Structure and photonic properties of a perylenediimide monolayer assembled by the Langmuir-Blodgett technique

Nicolas Fabre, Remigiusz Trojanowicz, Laureen Moreaud, Céline Fiorini-Debuisschert, Simon Vassant, Fabrice Charra

Structure and photonic properties of a perylenediimide monolayer assembled by the Langmuir-Blodgett technique

Nicolas Fabre,* Remigiusz Trojanowicz, Laureen Moreaud, Céline Fiorini-Debuisschert, Simon Vassant, Fabrice Charra *

Université Paris-Saclay, CEA-CNRS, Service de Physique de l'État condensé (SPEC), F-91191, Gif-sur-Yvette, France

* Corresponding authors

E-mail address: nicolas.fabre@cea.fr (N.Fabre), fabrice.charra@cea.fr (F.Charra)

Keywords: Langmuir-Blodgett, Monolayer, Absorption, Fluorescence

Abstract

The photonic responses of densely-packed dye molecule assemblies are strongly dependent on their organization and environment. The precise control of molecular orientations and distances relative to the substrate and to each other, is thus a key-point in the design of photonic molecular materials. Herein, we report the preparation of a homogeneous and well-organized single monolayer of perylenediimide derivative by means of the Langmuir-Blodgett technique. Its optical properties disclose an intense charge-transfer excitonic absorption band related to an important intermolecular coupling. Furthermore, an important immunity to photobleaching is observed for such a molecular assembly. The dipolar orientations of the molecules along the substrate have been unambiguously determined by angle of incidence resolved polarized absorption and by back focal plane fluorescence mapping. In addition, time-resolved spectroscopy reveals a fast two-dimensional diffusion of excitons consistent with a strong π-stacking of adjacent PDI molecules.

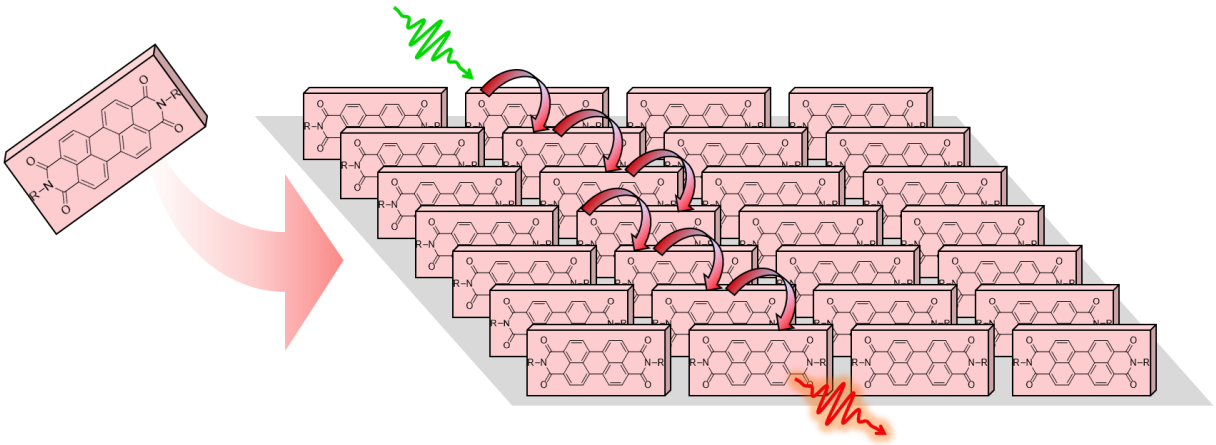

Introduction

The photonic properties of close-packed assemblies of dye molecules undergo significant differences as compared to isolated and diluted species.[1,2] McRae and Kasha were the first to report that these changes arise from near-field optical interactions.[3] Illustrative instances are the phenomena of aggregation-induced emission or enhanced emission, or the spectral shifts caused by self-association of dyes in solution.[4–6] Depending on the aggregation pattern of the dyes, either bathochromically-shifted J-bands or hypsochromically-shifted H-bands are generated, representing collective excitations and energy bands of delocalized excitons.[7–9] The substantial transition dipole moments associated with such excitations lead to enhanced optical interactions, enabling, for instance, a strong-coupling regime to be achieved with plasmon resonators.[10,11] Interactions between a dye and its surrounding environment at the molecular level can also trigger changes in its photonic properties. Conformation locking of the dye, or immersion in a polarizable medium, can induce shifts in the absorption or emission spectra.[12,13] Lastly, new intermolecular charge-transfer absorption peaks can be related to electron tunneling between π-conjugated systems which are close enough from each other. Thus, accurate control at the molecular scale of condensed dye assemblies is crucial for manipulating the optical response of matter and exploring novel photonic processes.[14]

Among dyes, perylenediimide (PDI) and its derivatives are widely used in several technological fields such as pigments,[15] photovoltaic cells,[16] optical switches,[17] lasers[18] and light-emitting diodes[19].[20] From a scientific point of view, they offer a paradigm platform both in the context of self-organization, through 3D mesophases[21,22] or 2D surface self-assembly[23,24], and of solid-state electronic[25,26] and photonic[27,28] processes. The optical responses of PDIs are the result of a complex and subtle interplay between molecule-substrate and molecule-molecule interactions, of electronic or electromagnetic – especially near-field – nature. For example, it was recently reported that PDI derivatives with long alkyl chains are able to stack perpendicular to a gold substrate to form H-aggregates.[29] An intense absorption band related to this aggregation and assigned to charge-transfer exciton, was observed and a strong coupling regime between this transition and gold surface plasmon was demonstrated for thicknesses of 10 monolayers and above.[8] However, many photonic processes take place at monolayer coverages, thus offering valuable opportunities to study in more detail the interplay between molecular organization and specific optical processes. For example, the self-assembly of PDI stirred by the graphene atomic lattice has been shown to exhibit a characteristic signature in its absorption spectra.[30] Also, the inherent emission quenching by graphene through short-range electronic (Dexter) or longer-range electromagnetic (Forster) transfer can be tuned through a molecular pedestal concept controlling the distance and orientation of a PDI-derivative monolayer relative to graphene.[31] Hence, studies of the optical response of well-organized PDI monolayers are likely to provide deep insights into the role played by the various molecular couplings. It could provide a deep understanding of molecular structure and interactions, enabling the exploration of binding mechanisms and emergent properties at the nanoscale. In addition, such research has the potential to advance nanotechnology by facilitating precise control over molecular organization, leading to the development of innovative materials and nanoscale devices with tailored properties and applications.

Several techniques can be used for the deposition of PDI monolayers on a substrate. Although PDI seem far from the ideal amphiphilic structure typically involved in Langmuir-Blodgett (LB) deposition, this technique has been successfully applied to alkylated PDI derivatives.[32–36] The LB technique makes it possible to obtain new out-of-equilibrium structures unreachable through drop casting or sublimation, and thus appears complementary to such more conventional methods.[37]

Herein, we focused on N,N'-ditridecyl-3,4,9,10-perylenedicarboximide (**PDI-C_{13}** see Figure 1.*a*) deposited through the LB technique on a neutral glass substrate to focus on intermolecular couplings . We determined unambiguously and with accuracy how the molecules are organized on the glass surface and how this organization affects their photonic properties.

Materials and methods

Chemicals. N,N'-ditridecyl-3,4,9,10-perylenedicarboximide (**PDI-C_{13}**), chloroform and trifluoroacetic acid were obtained commercially from Sigma-Aldrich (Ref. 383783).

Langmuir-Blodgett. Monolayers were prepared using a Langmuir-Blodgett trough (KN2001 LB small, Biolin Scientific). The subphase was ultrapure water (18 MΩ cm) maintained at 20°C. A **PDI-C_{13}** solution (6×10^{-4} mol L^{-1} in a chloroform/trifluoroacetic acid mixture (9:1)) was spread onto the surface using a microsyringe (25 µL), and leaving 30 min for the solvent to evaporate.

For compression isotherms, the air-water interface was compressed with symmetric barriers at constant rate (25 mm min^{-1}). Surface pressure was continuously monitored using the Wilhelmy method.

For LB transfers, the monolayers were compressed to 25 mN m^{-1} and kept constant with the feedback of barriers going back and forth. Depositions of monolayers were done using *Z*-type, and a dipper speed of 2 mm min^{-1}. The substrates for monolayers were 175-µm thick glass cover plates (20×20 mm).

For micro-spectroscopy, one side of the glass cover plate is cleaned with Red First Contact Polymer (First Contact Polymer, Photonic Cleaning Technologies) to remove PDI deposits.

Steady-state micro-spectroscopy. Steady-state micro-spectroscopy was performed using an inverted optical microscope (IX71, Olympus) equipped with an objective lens (Nikon, 60×, 0.8 N.A.). The detection chain was made of an imaging spectrometer (Kymera 193i, Andor) equipped with a blazed grating (SR2-GRT-0150-0500, Andor) and a CMOS camera (Zyla 5.5, Andor). An automatized slit was positioned at the entrance of the spectrometer and tuned to a width of 10 µm. Hyperspectral 1D-images were obtained with a spectrum acquired every 0.1 µm along a 230-µm-long segment on the sample.

For micro-absorption, a white thermal lamp (12V 100W HAL-L, Olympus) was used to probe the sample. The reference was acquired on a clean glass cover plate. The transmitted signal was collected through the objective lens and sent to the detection chain to construct a 1D hyperspectral image.

For micro-emission, a 532 nm light (60 µW cm^{-2}) from a laser (Cobolt 532 08-01 series, Hubner photonics) was used to excite the sample. This excitation light was filtered (LL01-532, Semrock) and focused on the sample through the objective lens (Nikon, 60×, 0.8 N.A.). The retroemitted fluorescence was collected through the microscope objective, filtered with appropriate filters (LPD02-532-RU + LP03-532-RU, Semrock) and sent to the detection path to construct a hyperspectral 1D image.

Fluorescence quantum yield. Fluorescence quantum yield was measured on a Fluorolog-3-221 (Horiba Jobin Yvon) equipped with an integrating sphere (Quanta-*φ*, Horiba Jobin Yvon). The method developed by de Mello and coworkers was employed.[38]

Incidence-angle resolved absorption. Absorption spectra at various incidence angle were recorded on a QE-Pro Ocean Optics spectrophotometer. White light (MWWHL4, ThorLabs) was expanded and collimated using an achromatic doublet (AC254-100-A-ML, ThorLabs). Then, a diaphragm was used to obtain a beam size of 1 mm diameter on the sample. The polarization was controlled using a linear polarizer (LPVISC100, ThorLabs) to obtain *p* (i.e. Transverse-Magnetic) polarization. The incidence angle was tuned by rotating the sample holder from 0 to 70° (5° increments) and the spectrum was recorded at each angle.

Back focal plane imaging. The radiation patterns were acquired through back focal plane fluorescence imaging performed on a separate detection arm of the IX71 microscope using a

f=100 mm Bertrand lens. A diaphragm placed at the image plane permits to select a region of interest. The excitation source was a 532 nm (1.8 mW cm^{-2}) laser (CPS532, ThorLabs). The sample was directly illuminated by the 532 nm laser light. The fluorescence signal was collected through a microscope oil immersion objective lens (Nikon, 60×, 1.50 N.A.), filtered with appropriate filters (LPD02-532-RU + LP03-532-RU, Semrock and FB700-10, Thorlabs) and were detected by means of an EMCCD camera (Ixon Ultra, Andor) positioned at the focus of the Bertrand lens.

Correlated Atomic Force Microscopy (AFM) and fluorescence mapping. Simultaneous microfluorescence and AFM microscopy analyses were performed using a homemade set-up involving an inverted microscope (Olympus IX71, objective lens 40×, 0.95 N.A.) coupled to a cantilever type AFM platform (NanoWizard III, JPK) and associated to a picosecond supercontinuum laser excitation (NKT Photonics, SuperK EVO incorporating a SuperK Varia, NKT Photonics filtering module to select specific wavelength for irradiation λ=532 nm, Δλ~5 nm. Here it was also associated to a band-pass filter Thorlabs FLH532-4, for better filtering). Laser polarization together with average power can be controlled. AFM images were recorded in the intermittent-contact (tapping) mode under ambient conditions. Silicon cantilevers (ACTA, AppNano) were used with a nominal spring constant of 37 N m^{-1}, resonance frequency of 300 kHz. In order to correlate topographic and optical measurements, the preliminary alignment of the AFM tip with the laser spot at the focus is needed. The sample is then raster scanned enabling simultaneous topography (tapping mode) and photoluminescence recording. Important to note is that the two correlated images are obtained through two probes of different sizes (topography/AFM tip ~10 nm and luminescence/laser spot ~300 nm).

Time-resolved micro-spectroscopy. Fluorescence decay curves were obtained by time-correlated single-photon counting (TCSPC) using an inverted optical microscope (IX71, Olympus) equipped with an oil immersion objective lens (Nikon, 100×, 1.45 N.A). The setup was composed of a Supercontinuum laser (SuperK Evo, NKT Photonics) emitting pulses of 30-50 ps at 20 MHz repetition rate associated to a filter module (SuperK Varia, NKT Photonics) to select specific wavelength for irradiation (here, λ=532 nm, Δλ~5 nm). Excitation light is further filtered (LL01-532-12.5, Semrock), reflected by a semi-transparent plate and focused on the sample through the objective. The retroemitted fluorescence was collected by the same microscope objective and detected beyond a long-pass dichroic filter (BLP01-532R-25, Semrock), by means of a microchannel plate photomultiplier (MCP-PMT R3809 U-50, Hamamatsu), connected to a TCSPC module (PicoHarp 300, PicoQuant). The instrumental response was recorded with a FWHM (full width at half-maximum) of ~80 ps. Fluorescence decay data were finally processed with the help of IgorPro (Wavemetrics).

Estimation of the number of absorbed photons and excited molecules per laser pulse. The number of photons in the pump pulse per unit of surface was calculated from the measured pump energy (8.5×10^{-13} J) divided by the energy of a photon at the excitation wavelength (532 nm) providing a number of 2.3×10^{6} photons per unit of surface. Next, we assume that the incident beam is a 300 nm-diameter cylinder (i.e. close to the diffraction limit). The number of absorbed photons per surface unit in the excited volume is obtained by multiplying the number of photons in the pump pulse by the absorptance at 532 nm (3%, see microspectroscopy measurement), providing a number of 6.8×10^{4} photons absorbed. As the area per molecule is estimated to 55 $Å^2$ (see the compression isotherm), the number of molecules in illuminated volume is estimated to 5.1×10^{5}. The ratio of molecules excited per pulse in the pump area was found from the number of absorbed photons divided by the number of molecules and it is estimated to 12%.

Results and discussion

Langmuir-Blodgett. The compression isotherm of **PDI-C_{13}** is reported in Figure 1.*b*. Three regions are noticeable on this curve, one above 70 $Å^2$ $molecule^{-1}$, the second from 45 to 70 $Å^2$ $molecule^{-1}$ and

the last one beyond 45 $Å^2$ $molecule^{-1}$. As previously reported in the literature, the first low-pressure range corresponds to free molecules lying on the surface, while the range from 45 to 70 $Å^2$ $molecule^{-1}$ is related to the condensed phase.[35] The Langmuir film is transferred to glass substrate at a surface pressure of 25 mN cm^{-1} corresponding to a surface of 55 $Å^2$ $molecule^{-1}$ and resulting in a constant transfer ratio of 1. Three orientations of molecules on the surface can be considered, lying either flat on the surface, or edge-on or head-on, as schematized on Figure 1.*c*. For PDI self-assembled onto graphene, the area per molecule is reported to be 222 $Å^2$ $molecule^{-1}$ in a flat orientation as shown by STM.[30] In our case, the area per molecule is four times smaller, so this possibility of a flat geometry can be reasonably dismissed. As for the last two orientations, accounting for experimental uncertainties, their projected areas are both consistent with the area used for the transfer. To unambiguously determine the orientation of the molecules on the surface, we performed optical characterizations.

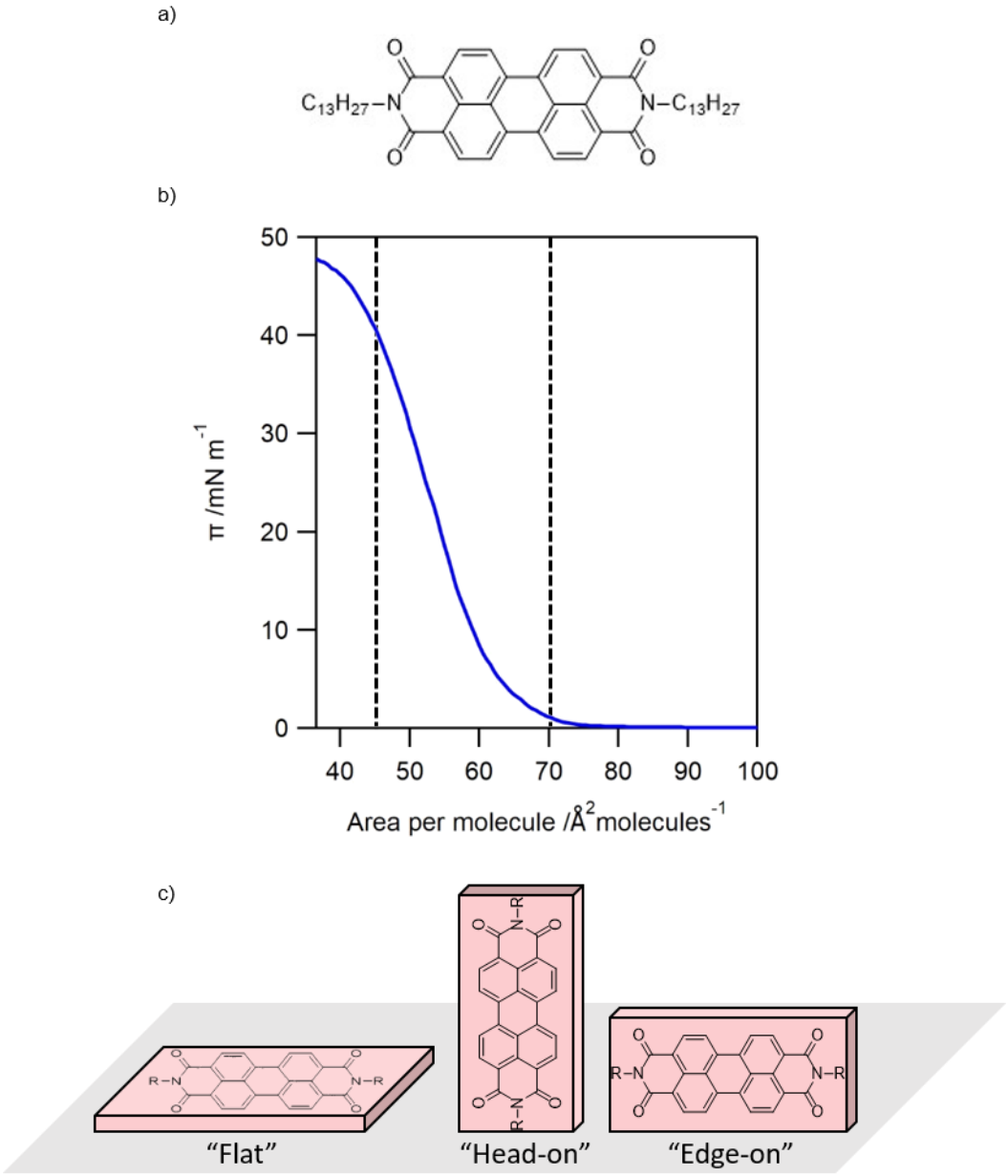

Figure 1. a) Molecular structure of ***PDI-C$_{13}$****; b) Isotherm for the first compression of* ***PDI-C$_{13}$*** *using a compression rate of 25 mm* min^{-1} *and 20 °C as subphase temperature. c) Possible orientations for* ***PDI-C$_{13}$*** *on glass substrate after transfer.*

Micro-spectroscopy

The hyperspectral image in absorption is shown in Figure 2.*a* and the average absorption spectrum is presented in Figure 2.*b*. First, we can observe that the absorption is homogeneous all along the segment, reflecting a uniform deposition, free from aggregation down to optical resolution scale (~0.5 µm). We can notice three absorption bands continuously present along the 230-µm-long segment: one extending from 555 to 670 nm with a maximum at 576 nm, the second one ranging from 515 to 555 nm, and the last one extending below 515 nm. It was previously reported for a similar PDI system that the lowest-energy band can be assigned to a charge transfer (CT) exciton.[8,29] This excitonic peak is a typical signature for the formation of a charge transfer Frenkel exciton with large oscillator strength, providing a strong indication for strongly π-π stacked conjugated moieties. The band with a maximum at 530 nm can be assigned to the $S_0 \rightarrow S_1$ electronic transition. At this wavelength, the absorptance is estimated to 3% as reported in Figure 2.*b*. Since the molar absorption coefficient is about $\sim 6.5 \times 10^4$ mol^{-1} L cm^{-1}, the cross section can be estimated to $\sim 1.2 \times 10^{-16}$ cm^2 molecule^{-1}.[22,30,39] Combining the sample absorbance and the molecule absorption cross section lead to an area of 40 Å^2 molecule^{-1}. This value is in agreement, within experimental errors, with the area of 55 Å^2 molecule^{-1} chosen for the Langmuir-Blodgett deposition with a unity transfer ratio. The CT excitonic peak is only related to an intermolecular π-π interaction and does not form through molecules-substrate interaction.[30] The presence of such peak coupled to the monolayer absorbance and density allows us to definitively reject the hypothesis of **PDI-C$_{13}$** conjugated core lying flat on the surface. At this point, the molecules are strongly π-stacked, which can only occur in either "edge-on" or "head-on" geometry.

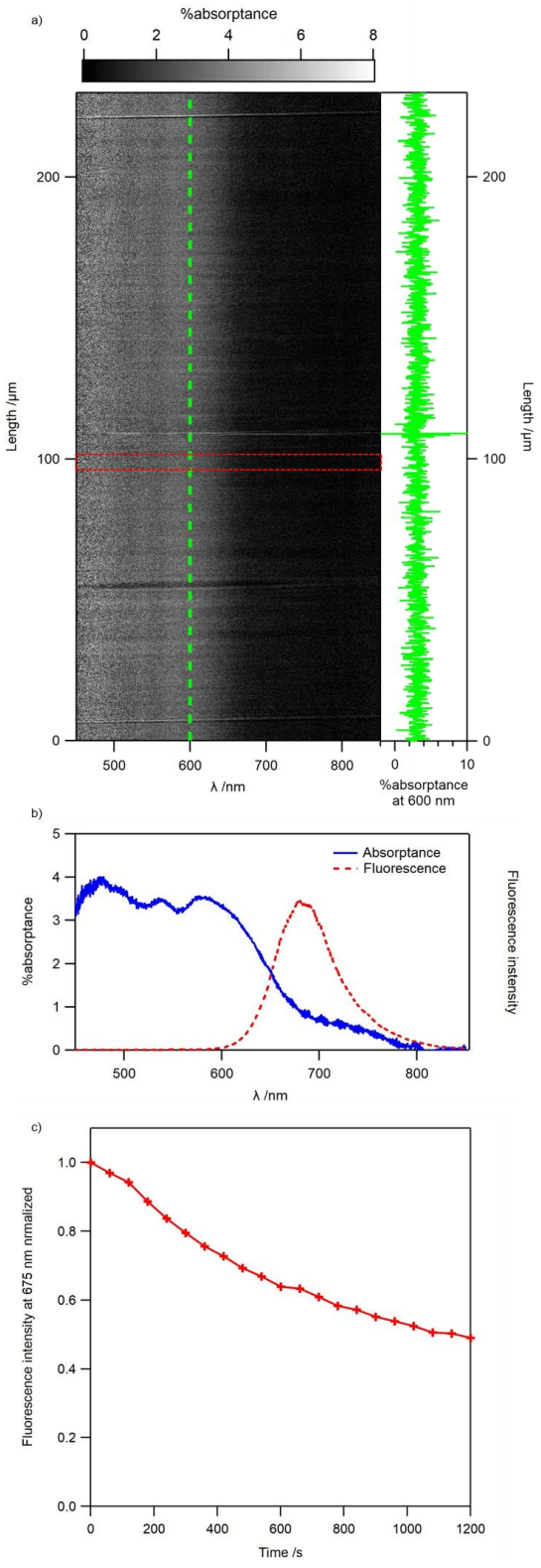

Figure 2. a) Hyperspectral image in absorption of ***PDI-C$_{13}$*** *monolayer on a 230-µm-long segment, and variations of absorptance at 600 nm (green line). b) Average absorptance (blue solid line, 230-µm-long segment) and emission (red dotted line, λ_{exc}=532 nm, area probed indicated by red rectangle on hyperspectral image 5 µm line) spectra. c) Evolution of the fluorescence maximum at 675 nm under CW irradiation at 532 nm (P=30 µW) for 20 minutes*

As concerns photoluminescence, (λ_{exc}=532 nm), the excitation spot delimits a small excitation area (5 µm), indicated by a rectangle on the hyperspectral image (Figure 2.*a*). The emission spectrum is plotted in Figure 2.*b*. A broad emission band, ranging from 600 to 850 nm with a maximum at 670 nm

is observed. The fluorescence quantum yield for **PDI-C$_{13}$** monolayer was estimated in an absolute way to 5.5±0.5 %. This value is consistent with previous observations that PDI derivatives have their emission weakened by strong π-π stacking.[17] Photobleaching of such monolayer was studied under excitation at 532 nm with a power of 30 µW. The evolution of fluorescence intensity at 675 nm is presented in Figure 2.*c*. After 20 min of irradiation, a 50 % loss of the initial fluorescence was noticed. The number of absorption/relaxation cycles was then estimated to ~10^{11}. This value indicates a quite remarkable photostability for a single monolayer, as compared to molecules in solution.[40,41] To explain this unexpected photostability, we suggest that long hydrophobic alkyl chains lie above the less hydrophobic PDI cores and help to prevent photobleaching of the PDI core by acting as a barrier to surrounding dioxygen. Moreover, the proximity imposed by the strong π-π stacking interaction of **PDI-C$_{13}$** can also prevent the contact with dioxygen.

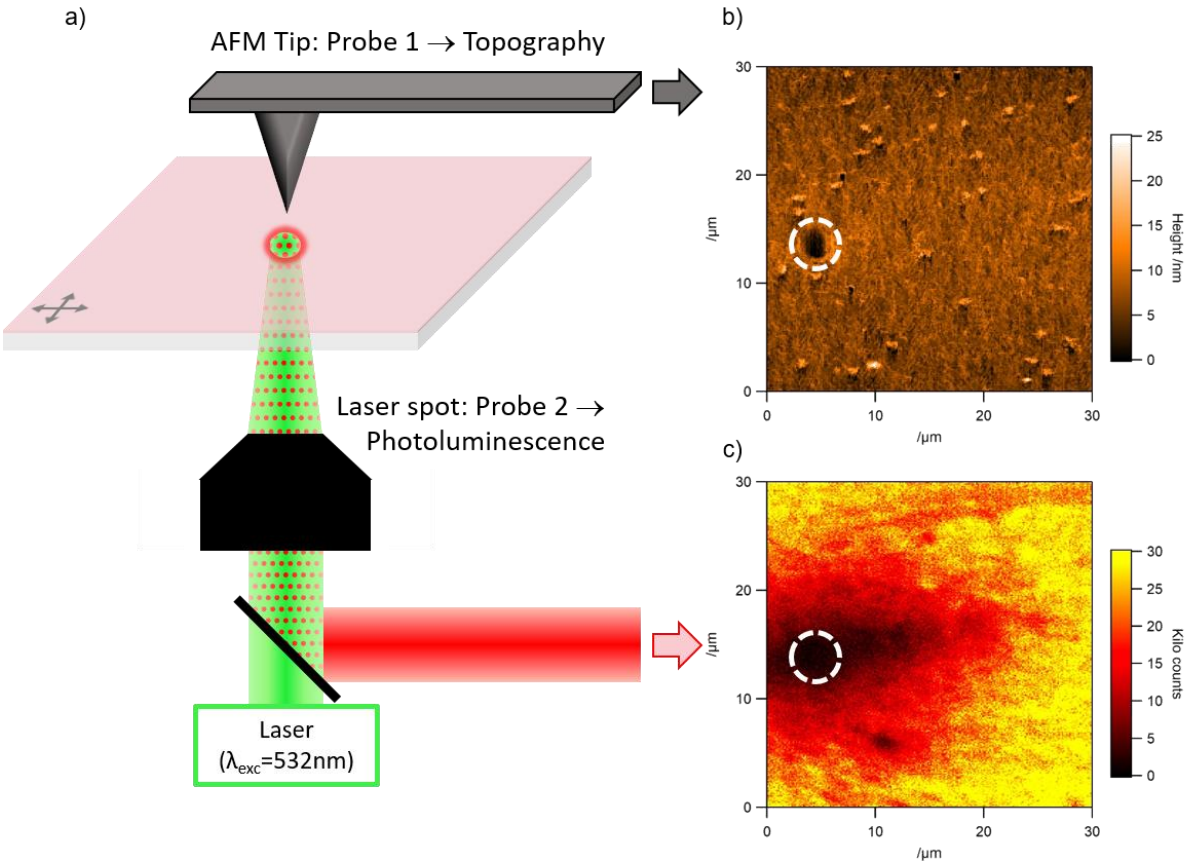

Figure 3. a) Simplified scheme of the correlated AFM and fluorescence microscopy set-up. The excitation laser beam (532 nm, ~0.3 µW average power) is linearly polarized in the plane of the sample. After reflexion onto a dichroic mirror (SemRock Di02-R532-25x36), it is focused onto the sample using a 40x, ON 0.95 microscope objective. The emitted luminescence is collected through the same microscope objective and reflected by a dichroic mirror (SemRock FF735-Di670-25x36), passing through a long pass filter (SemRock BL02-561R-25) before detection by a channel plate multiplier working in the photon counting mode (Perkin Elmer MP-993-CL). b) Topography and c) photoluminescence map of the same area. The dotted circles correspond to a purposely photobleached area, serving as a landmark to check the correlation between optical and topography images

AFM measurement

Micro-spectroscopy provides us with information regarding the homogeneity of absorption. Correlative morphology and confocal fluorescence measurements were also performed to check the sample structural and emission homogeneity as shown in Figure 3.*b* and *c* respectively. For this purpose, we employed a correlative AFM and fluorescence microscopy set-up as depicted in Figure 3.*a*. In topography, it can be noticed that no defects such as aggregates are observed on the probed area. The RMS roughness is quite low (<3 nm) and the peak-to-valley roughness is estimated to 30 nm. This corresponds to the roughness that was measured on the glass cover slide itself. In the absence of any defects and in order to ensure that the same area is probed in topography and emission, a small area was purposely photobleached in order to check the alignment of the two probes (see white dotted circle in Figure 3b-c). As seen in figure 3d, a quite homogeneous photoluminescence is observable, with micronic domains of slightly varying photoluminescence intensity most probably corresponding to molecular domains of slightly varying molecular alignment. These two images, topography and fluorescence mapping, further confirm the micro-spectroscopy observations. From these observations, we can assume that the sample prepared via Langmuir-Blodgett technique is homogenous in density and organization on a large-scale range.

Photoluminescence radiation pattern.

Collecting the radiation pattern of the photoluminescence in the back focal plane allows getting insights into the orientation of the transition dipole moment of the molecules.[42] In the case of the perylene derivative, both S_0-S_1 absorption and S_1-S_0 emission transition moments are collinear with the N-N axis.[43] The theoretical simulations of the radiation patterns for a single dipolar molecule oriented either in the plane or perpendicular to the plane of the substrate are shown in Figure 4.*a* and *b* respectively.[42] For a transition moment contained in the plane of the substrate, two lobes of maximum intensity are observed, while at 90° there are two minima. For dipoles that are strictly perpendicular to the plane, there is a toric zone of maximum intensity and in the center no light is detected. In our case, the sample was irradiated at an angle of 40° and the full objective field-of-view was probed. The polarization of the laser light is either *s* (TE) or *p* (TM). The experimental radiation patterns of the collection of molecules obtained for each of the two polarizations are depicted in Figure 4.*c* and *d* respectively. For *s* polarization, the collected pattern is very similar to that corresponding to a dipole oriented in the plane of the substrate. For this polarization, the excitation electric field is in-plane and excites most efficiently molecules with a transition moment in the plane. Then a pattern very close to the theoretical one for an in-plane single molecule indicates that the collections of molecules are all oriented in the in-plane direction. More meaningfully, for p polarization, molecules with perpendicular moments of transition are excited with nearly equal probability than in-plane molecules (~45 %-55% resp.). The pattern obtained is still very similar to that of a purely in-plane dipole. This indicates that the molecules are all oriented highly parallel to the substrate.

In addition, the line profiles of the maximum and minimum directions are plotted and compared with the theoretical one for a single molecule as shown in Figure 4.*e.f.g*. For *s* and *p* polarizations the results of these line profiles are very similar. The values of the local maxima are reached for similar angles. Moreover, the line profiles are similar to the theoretical ones. For the profiles along the maxima of interest, the value of the minimum is closer to zero for the theoretical than for the experimental results. It is for the profiles along the minimum intensity lobes that the differences are most marked. These differences can be explained by the collection of molecules with different azimuthal directions within the substrate plane in the experimental case. Extinction is normally expected for both lobes, but in the case of the monolayer it is simply a local minimum that is reached. Hence, the radiation patterns indicate that the molecules are mainly organized with their transition moment collinear to the glass substrate, that is "edge-on" since the planar geometry has been ruled out based on the area per molecule and the existence of CT excitons.

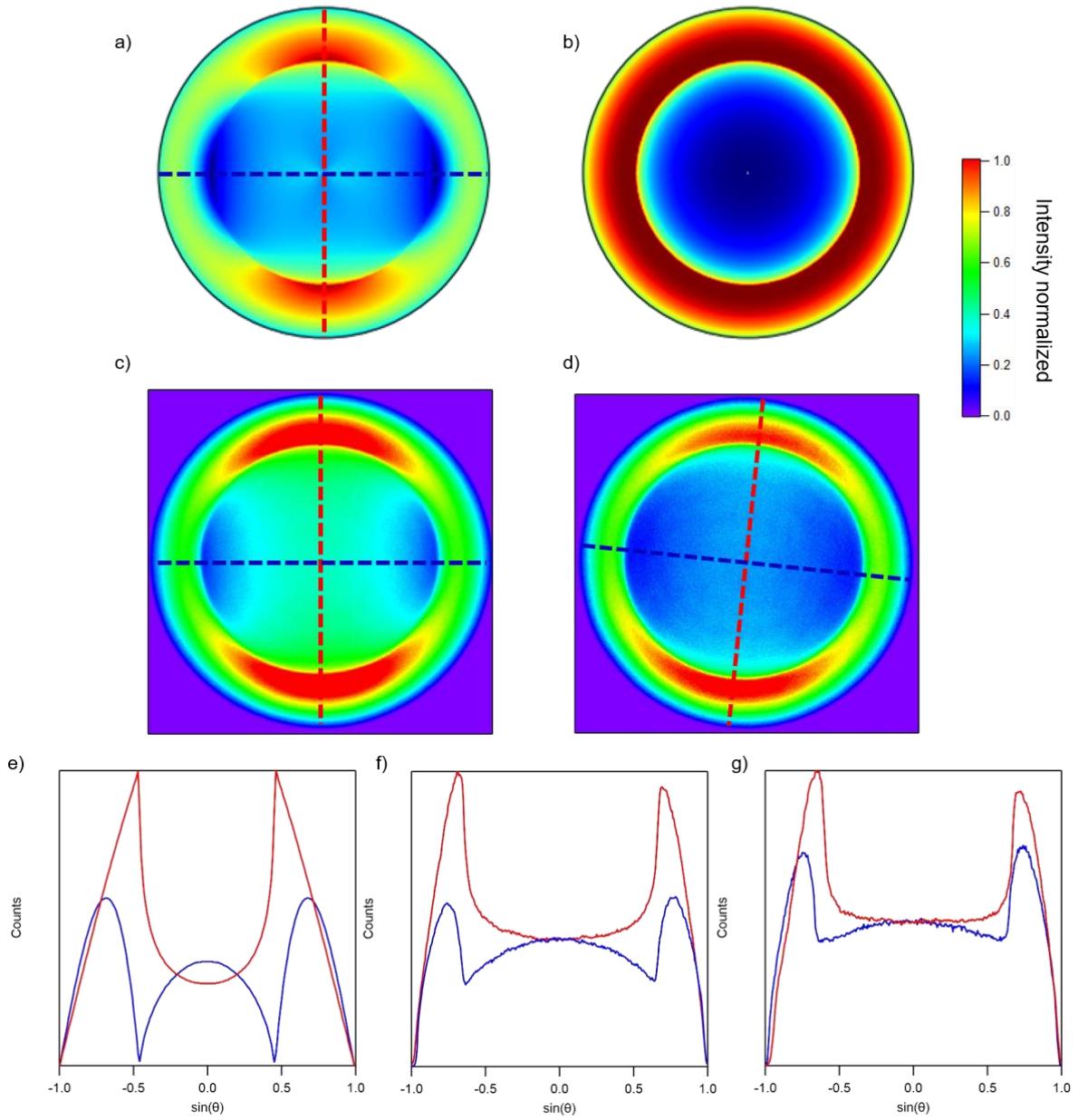

Figure 4. Calculated emission patterns of a single dipole at an air-glass interface in the back focal plane of a N.A.=1.5 objective lens for a) a in plane dipole and b) a dipole perpendicular to the plane. Observed pattern for a ***PDI-C$_{13}$*** *monolayer under excitation at 532 nm for c) s-polarization and d) p-polarization. Cross sections along the maximum (red line) and minimum (blue line) intensity lobes for e) calculated emission pattern of an in-plane dipole, f) for emission pattern recorded at s-polarization and g) for emission pattern recorded at p-polarization.*

Incidence angle resolved absorption spectroscopy

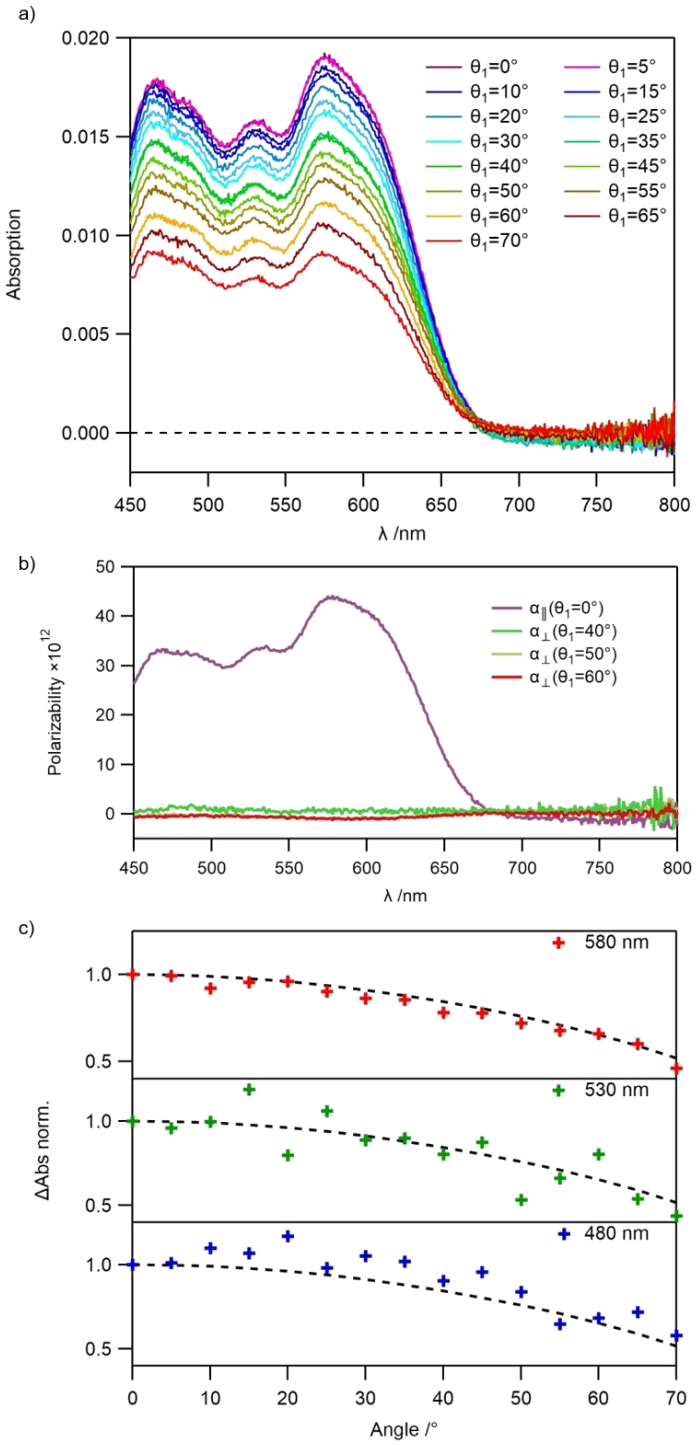

Figure 5. a) Absorption spectra of ***PDI-C$_{13}$*** *monolayer at several incidence angle. b) Polarizability contribution in the plane ($\alpha_{\parallel}$, purple line) and perpendicular to the plane for several incidence angle ($\alpha_{\perp}$, green line for θ_1=40 °, yellow line for θ_1=50 ° and red line for θ_1=60 °)). c) Evolution of the absorption at 580 nm (red cross), 530 nm (green cross) and 480 nm (blue cross) as function of incidence angle with its theoretical evolution (black dotted line).*

To further determine and confirm the orientation of molecules on the surface, we have carried out incidence-angle resolved absorption spectroscopy.[44] The probe white light beam is polarized horizontally, that is *p* (TM), the sample being vertical, and absorption spectra are recorded for several incidence angle θ_1 of the probe light. Figure 5**Erreur ! Source du renvoi introuvable.**.*a* presents the absorption spectra obtained for several angle of incidence for a glass substrate covered on both sides

with a LB-deposited **PDI-C$_{13}$** monolayer. As expected, the absorption line profile of the different spectra is similar to the one obtained in micro-spectroscopy, the CT excitonic band is well resolved as the other two bands related to vibronic-electronic transitions. As the angle of incidence increases, the intensity of all the bands in the spectrum decreases uniformly. Initially, at normal incidence θ_1=0, the polarization is in the plane, and only those molecules that have a transition moment in the plane absorb light. When the incidence angle increases, the molecules in the plane absorb less light, whereas molecules with transition moments perpendicular to the plane should start to absorb light. In our case, only a decrease is observed, which confirms that there are mainly molecules that are arranged in the plane. From these spectra it is possible to obtain the absorption contribution, i.e. the imaginary part of the surface polarizability tensor elements in the plane $\alpha_{\parallel}$ and out of the plane $\alpha_{\perp}$. For $\alpha_{\parallel}$ only the absorption spectra at incidence angle θ_1=0° is required and it is determined as follows:

$$Im(\alpha_{\parallel}) = \frac{\lambda\varepsilon_0}{2\pi}\mathrm{Abs}(\lambda, \theta_1 = 0)(n_1 + n_2) \qquad \text{(Eq.1)}$$

Introducing λ; the wavelength, ε_0; the vacuum permittivity, and Abs(λ,θ_1=0) the absorption spectra recorded at normal incidence. The shape of $Im(\alpha_{\parallel})$ is displayed in Figure 5**Erreur ! Source du renvoi introuvable.**.*b*. As for the absorption spectrum, three bands are observed meaning that transition moments in the plane account for these three absorption bands.

Regarding $Im(\alpha_{\perp})$, it can then be estimated from $Im(\alpha_{\parallel})$ and the absorption spectra at high angle of incidence (e.g. θ_1=50 °) using the following formula:

$$Im(\alpha_{\perp}) = \left[\frac{\lambda\varepsilon_0}{2\pi}\mathrm{Abs}(\lambda, \theta_1 = 0) - \frac{Im(\alpha_{\parallel})}{\frac{n_1}{\cos\theta_1} + \frac{n_2}{\cos\theta_2}}\right] \times \frac{\frac{\cos\theta_1}{n_1} + \frac{\cos\theta_2}{n_2}}{n_1 \sin\theta_1 \, n_2 \sin\theta_2} \qquad \text{(Eq.2)}$$

With θ_2; the refracted angle (related to incident angle θ_1 by the Snell law), n_1; the index of air, and n_2; the index of the substrate on which the monolayers are deposited. $Im(\alpha_{\perp})$ is represented in Figure 5**Erreur ! Source du renvoi introuvable.**.*b* for 40, 50 and 60° incidence angles. Whatever the angle used, it is uniformly close to zero, meaning that there is no contribution to the absorption perpendicular to the plane. The absorption spectrum is only due to the in-plane tensor component $Im(\alpha)$ implying that the transition moments of the molecules are mainly parallel to the glass substrate.

As an illustration, the normalized variations of the absorption at 580, 530 and 480 nm as a function of the angle of incidence are plotted in Figure 5**Erreur ! Source du renvoi introuvable.**.*c*. For each wavelength, the absorption decreases as the angle increases. This in agreement with the determination of $Im(\alpha_{\parallel})$ and $Im(\alpha_{\perp})$. Quantitatively, from the dispersion of the displayed wide-angle values of $Im(\alpha_{\perp})$, we can estimate that it is less than 3% of $Im(\alpha_{\parallel})$ corresponding to an angle larger than 80° from the normal to the substrate plane. In the case of a monolayer with a polarizability in the plane $Im(\alpha_{\parallel})$, the variation of the absorption as a function of angle of incidence θ_1 can be expressed as:

$$\Delta\mathrm{Abs} = \frac{1}{\frac{n_1}{\cos\theta_1} + \frac{n_2}{\cos\theta_2}} \qquad \text{(Eq.3)}$$

The expression in (Eq.3) was used to perform a curve fit on the evolution of absorption as shown in Figure 5**Erreur ! Source du renvoi introuvable.**.*c* and provide satisfactory results. These results reinforce our conclusion that the transition moment of **PDI-C$_{13}$** is in-plane and the molecule in the "edge-on" geometry.

Fluorescence decay.

To explore the dynamics of excited states of such **PDI-C_{13}** assembly, fluorescence decay measurements were conducted by means of the time-correlated single photon counting (TCSPC) technique. Fluorescence decays of the same area are plotted in Figure 6.*a* for various pump powers. A strongly pump-dependent multi-exponential decay is observed. Concerning the times below 1 ns, as the pump intensity is increased, a faster decay appears. The pump-power dependence of the decay points to an exciton-exciton annihilation process which, besides bulk media, can occur in 2D materials.[45–48] Excitons diffuse along the surface and when two excitons are close enough to interact, they fuse to form a single higher energy exciton. After 1 ns, a mono-exponential fluorescence decay is observed with a time constant independent of the pump power. This part of the decay, which corresponds to low residual densities of excitons is not affected by the exciton-exciton recombination and thus provides the intrinsic fluorescence lifetime τ_F.

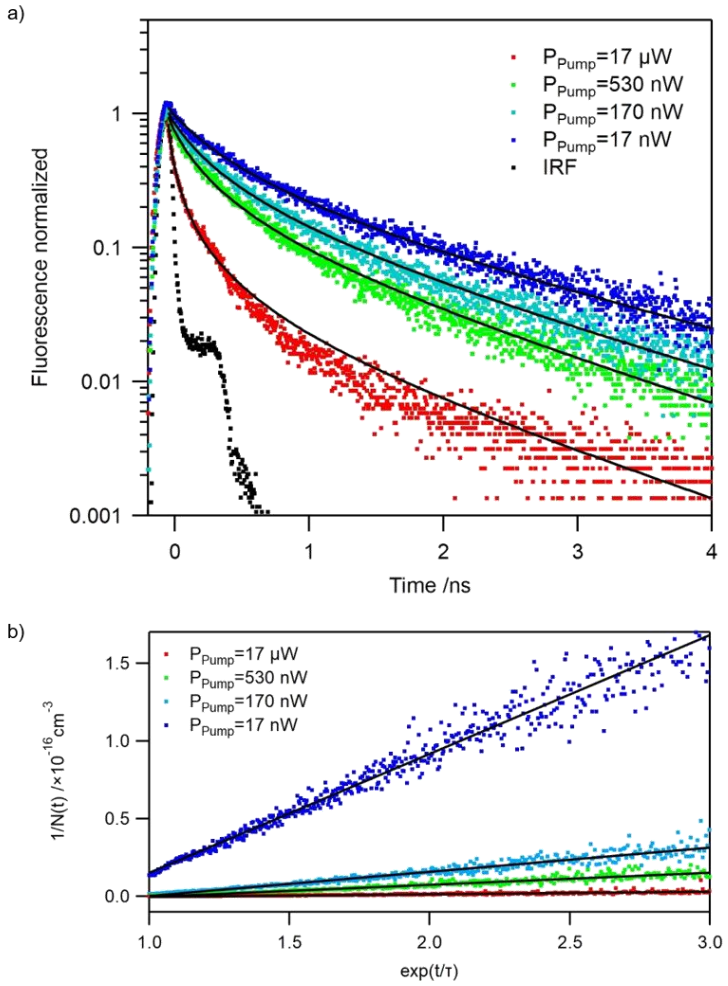

*Figure 6. a) Fluorescence decays for **PDI-C_{13}** monolayer at various pump power (dots) measured at λ_{exc}=532 nm and curve fitting (black lines and instrumental response (IRF, black dots)). b) Inverse of exciton density N(t) as function of exp(t/τ) at several pump power (dots) and curve fitting (black lines).*

To account for shorter time phenomenon, the fluorescence decay rate of the exciton population N is modeled in the literature and is described by the equation:[47]

$$\frac{dN(t)}{dt} = -\frac{N(t)}{\tau_F} - \gamma N(t)^2 \qquad \text{(Eq.4)}$$

Introducing γ the exciton-exciton annihilation constant. The solution of (Eq.4) can be expressed as:

$$N(t) = \frac{N_0 \exp\left(-\frac{t}{\tau}\right)}{1 + \gamma\tau N_0[1 - \exp\left(-\frac{t}{\tau}\right)]} \quad \text{(Eq.5)}$$

With N_0; the initial exciton density right after the excitation pulse determined as:

$$N_0 = \frac{4\lambda_{\text{exc}}}{\pi d^2 hc} \frac{P(10^{Abs_{\lambda_{\text{exc}}}})}{f} \quad \text{(Eq.6)}$$

With λ_{exc}; the wavelength of irradiation, d; the diameter of the excitation spot, h; the Planck constant, c; the velocity of light, P; the average power of irradiation, $Abs_{\lambda_{exc}}$; the absorption at irradiation wavelength, f; the repetition rate of the excitation laser pulses.

Curve fitting was performed using Eq.5 and provided satisfactory results for the three lowest powers. Values obtained for τ_F at different pump power are gathered into Table 1. For a pump power of 17 µW, the curve fitting is not so well satisfying at the beginning of the decay; a strong decrease is observed during the irradiation pulse, but the mono-exponential one provides a time that is in the same range as the other decays. Furthermore, almost the same fluorescence lifetime is obtained for the four decays, that can be estimated to τ_F~1.5 ns. Other decays measured at various locations on the sample were recorded with a pump probe of 170 nW and fitted using Eq.5 and they result in similar values for the fluorescence lifetime. Concerning the annihilation constant rate γ, it is possible to determine it using (Eq.7):

$$\frac{1}{N(t)} = \left[\frac{1}{N_0} + \gamma\tau\right] \exp\left(\frac{t}{\tau}\right) - \gamma\tau \quad \text{(Eq.7)}$$

The inverse of exciton density is expected to vary linearly as function of exp(t/τ) with an intercept and slope related to γ. The black lines in Figure 6.*b* were calculated using (Eq.7) and provides values of γ. It is ranging from 3.8×10^{-10} to 8.0×10^{-12} cm^2 s^{-1} and appears dependent of the pump power employed. At high pump power, observed decay constants become inconsistent due to a dynamics faster than instrumental pulse response (Figure 6.*a*). Further studies of the excited states will be carried out using other pump power and sorting photons per wavelength to provide more complete information about this original exciton diffusion process in a 2D system.

Table 1. Corresponding values of pump power, number of molecules excited per pulse, initial exciton density N_0 and values of fluorescence lifetime τ_F and annihilation constant rate γ determined.

Pump power /nW	Number of molecules excited per pulse /%	N_0 /cm^{-2}	τ_F /ns	γ /cm^2 s^{-1}
17	1.3×10^{-2}	3.3×10^{10}	1.8±0.05	3.8×10^{-10}
170	1.3×10^{-1}	3.3×10^{11}	1.5±0.02	7.5×10^{-11}
530	4.5×10^{-1}	1.0×10^{12}	1.39±0.03	3.9×10^{-11}
17 000	13	3.3×10^{13}	1.32±0.06	8.0×10^{-12}

Conclusion. In conclusion, we have prepared a **PDI-C$_{13}$** monolayer using the Langmuir-Blodgett technique. This monolayer exhibits a bright red-shifted emission and an intense charge-transfer excitonic absorption band related to a strong π-π interaction between PDI cores. The resistance to photobleaching appears very strong for such a monolayer assembly and the sample is very homogeneous. We also conducted a comprehensive study of the orientation of the molecules on the surface of the glass. Photoluminescence radiation patterns and angle of incidence resolved absorption spectroscopy converge toward an in-plane "edge-on" orientation of the molecules. Then, area-per-molecule arguments, reinforced by various signatures of π-π intermolecular interactions allowed us to

conclude for an "edge-on" arrangement on the glass substrate. Finally, we have shown that such an arrangement exhibits an efficient exciton-exciton annihilation following a 2D diffusion process.

Acknowledgements

We thank Rémi Métivier for his help in the determination of fluorescence quantum yield. The authors acknowledge the support of the French Agence Nationale de la Recherche (ANR), under grants ANR-21-CE06-0041 (project LESOMMETA) and ANR-18-CE09-0030 (project STACSAMGRAPH) .

References

(1) Oelkrag, D.; Egelhaaf, H.-J.; Gierschner, J.; Tompert, A. Electronic Deactivation in Single Chains, Nano-Aggregates and Ultrathin Films of Conjugated Oligomers. *Synth. Met.* **1996**, *76* (1–3), 249–253.

(2) Gierschner, J.; Shi, J.; Milián- Medina, B.; Roca- Sanjuán, D.; Varghese, S.; Park, S. Luminescence in Crystalline Organic Materials: From Molecules to Molecular Solids. *Adv. Opt. Mater.* **2021**, *9* (13), 2002251.

(3) McRae, E. G.; Kasha, M. Enhancement of Phosphorescence Ability upon Aggregation of Dye Molecules. *J. Chem. Phys.* **1958**, *28* (4), 721–722.

(4) Lim, S.-J.; An, B.-K.; Jung, S. D.; Chung, M.-A.; Park, S. Y. Photoswitchable Organic Nanoparticles and a Polymer Film Employing Multifunctional Molecules with Enhanced Fluorescence Emission and Bistable Photochromism. *Angew Chem Int Ed.* **2004**, *46* (46), 6346-6350.

(5) He, Z.; Ke, C.; Tang, B. Z. Journey of Aggregation-Induced Emission Research. *ACS Omega* **2018**, *3* (3), 3267–3277.

(6) Würthner, F.; Kaiser, T., E.; Saha-Möller, C. R. J-Aggregates: From Serendipitous Discovery to Supramolecular Engineering of Functional Dye Materials. *Angew. Chem. Int. Ed.* **2011**, *50* (15), 3376–3410.

(7) Spano, F. C. Excitons in Conjugated Oligomer Aggregates, Films, and Crystals. *Annu. Rev. Phys. Chem.* **2006**, *57*, 217–243.

(8) Spano, F. C. The Spectral Signatures of Frenkel Polarons in H- and J-Aggregates. *Acc. Chem. Res.* **2010**, *43* (3), 429–439.

(9) Oleson, A.; Zhu, T.; Dunn, I. S.; Bialas, D.; Bai, Y.; Zhang, W.; Dai, M.; Reichman, D. R.; Tempelaar, R.; Huang, L.; Spano, F. C. Perylene Diimide-Based Hj- and HJ-Aggregates: The Prospect of Exciton Band Shape Engineering in Organic Materials. *J. Phys. Chem. C* **2019**, *123* (33), 20567–20578.

(10) Dintinger, J.; Klein, S.; Bustos, F.; Barnes, W. L.; Ebbesen, T. W. Strong Coupling between Surface Plasmon-Polaritons and Organic Molecules in Subwavelength Hole Arrays. *Phys. Rev. B* **2005**, *71* (3), 035424.

(11) Fofang, N. T.; Park, T.-H.; Neumann, O.; Mirin, N. A.; Nordlander, P.; Halas, N. J. Plexcitonic Nanoparticles: Plasmon−Exciton Coupling in Nanoshell−J-Aggregate Complexes. *Nano Lett.* **2008**, *8* (10), 3481–3487.

(12) Goujon, A.; Colom, A.; Straková, K.; Mercier, V.; Mahecic, D.; Manley, S.; Sakai, N.; Roux, A.; Matile, S. Mechanosensitive Fluorescent Probes to Image Membrane Tension in Mitochondria, Endoplasmic Reticulum, and Lysosomes. *J. Am. Chem. Soc.* **2019**, *141* (8), 3380–3384.

(13) Klymchenko, A. S. Solvatochromic and Fluorogenic Dyes as Environment-Sensitive Probes: Design and Biological Applications. *Acc. Chem. Res.* **2017**, *50* (2), 366–375.

(14) Markovitsi, D.; Pfeffer, N.; Charra, F.; Nunzi, J.-M.; Bengs, H.; Ringsdorf, H. Charge-Transfer Complexes of Discogenic Molecules : A Time-Resolved Study Based on Kerr Ellipsometry. *J. Chem. Soc. Faraday Trans.* **1993**, *89* (1), 37.

(15) Herrmann, A.; Müllen, K. From Industrial Colorants to Single Photon Sources and Biolabels: The Fascination and Function of Rylene Dyes. *Chem. Lett.* **2006**, *35* (9), 978–985.

(16) Li, C.; Yum, J.; Moon, S.; Herrmann, A.; Eickemeyer, F.; Pschirer, N. G.; Erk, P.; Schöneboom, J.; Müllen, K.; Grätzel, M.; Nazeeruddin, M. K. An Improved Perylene Sensitizer for Solar Cell Applications. *ChemSusChem* **2008**, *1* (7), 615–618.
(17) Ikariko, I.; Deguchi, S.; Fabre, N.; Ishida, S.; Kim, S.; Kurihara, S.; Métivier, R.; Fukaminato, T. Highly-Stable Red-Emissive Photochromic Nanoparticles Based on a Diarylethene-Perylenebisimide Dyad. *Dyes Pigments* **2020**, *180*, 108490.
(18) Ramirez, M. G.; Pla, S.; Boj, P.; Villalvilla, J.; Quintana, J.; Diaz-Garcia, M.; Fernandez-Lazaro, F.; Sastre-Santos, A. 1,7-Bay-Substituted Perylenediimide Derivative with Outstanding Laser Performance. *Adv. Opt. Mater.* **2013**, *1* (12), 933–938.
(19) Dayneko, S. V.; Rahmati, M.; Pahlevani, M.; Welch, G. C. Solution Processed Red Organic Light-Emitting-Diodes Using an *N* -Annulated Perylene Diimide Fluorophore. *J. Mater. Chem. C* **2020**, *8* (7), 2314–2319.
(20) Würthner, F.; Saha-Möller, C. R.; Fimmel, B.; Ogi, S.; Leowanawat, P.; Schmidt, D. Perylene Bisimide Dye Assemblies as Archetype Functional Supramolecular Materials. *Chem. Rev.* **2016**, *116* (3), 962–1052.
(21) Struijk, C. W.; Sieval, A. B.; Dakhorst, J. E. J.; van Dijk, M.; Kimkes, P.; Koehorst, R. B. M.; Donker, H.; Schaafsma, T. J.; Picken, S. J.; van de Craats, A. M.; Warman, J. M.; Zuilhof, H.; Sudhölter, E. J. R. Liquid Crystalline Perylene Diimides: Architecture and Charge Carrier Mobilities. *J. Am. Chem. Soc.* **2000**, *122* (45), 11057–11066.
(22) Balakrishnan, K.; Datar, A.; Naddo, T.; Huang, J.; Oitker, R.; Yen, M.; Zhao, J.; Zang, L. Effect of Side-Chain Substituents on Self-Assembly of Perylene Diimide Molecules: Morphology Control. *J. Am. Chem. Soc.* **2006**, *128* (22), 7390–7398.
(23) Krukowski, P.; Tsuzuki, T.; Minagawa, Y.; Yajima, N.; Chaunchaiyakul, S.; Akai-Kasaya, M.; Saito, A.; Miyake, Y.; Katayama, M.; Kuwahara, Y. Detection of Light Emission from (*S*)-PTCDI Molecules Adsorbed on Au(111) and NiAl(110) Surfaces Induced by a Scanning Tunneling Microscope. *J. Phys. Chem. C* **2016**, *120* (7), 3964–3977.
(24) Xiao, Y.; Tao, J.; Peng, X.; Song, Y.; Lei, P.; Xu, H.; Xiao, X.; Tu, B.; Zeng, Q. Two-Dimensional Molecular Network Built from Hierarchy Self-Assembly of Perylene Bisimide Derivatives. *ACS Appl. Mater. Interfaces* **2021**, *13* (14), 17129–17138.
(25) Tatemichi, S.; Ichikawa, M.; Koyama, T.; Taniguchi, Y. High Mobility N-Type Thin-Film Transistors Based on N,N′-Ditridecyl Perylene Diimide with Thermal Treatments. *Appl. Phys. Lett.* **2006**, *89* (11), 112108.
(26) Felter, K. M.; Caselli, V. M.; Günbaş, D. D.; Savenije, T. J.; Grozema, F. C. Interplay between Charge Carrier Mobility, Exciton Diffusion, Crystal Packing, and Charge Separation in Perylene Diimide-Based Heterojunctions. *ACS Appl. Energy Mater.* **2019**, *2* (11), 8010–8021.
(27) Lin, M.-J.; Jiménez, Á. J.; Burschka, C.; Würthner, F. Bay-Substituted Perylene Bisimide Dye with an Undistorted Planar Scaffold and Outstanding Solid State Fluorescence Properties. *Chem. Commun.* **2012**, *48* (99), 12050.
(28) Azarova, N.; Ferguson, A. J.; van de Lagemaat, J.; Rengnath, E.; Park, W.; Johnson, J. C. Coupling between a Molecular Charge-Transfer Exciton and Surface Plasmons in a Nanostructured Metal Grating. *J. Phys. Chem. Lett.* **2013**, *4* (16), 2658–2663.
(29) Bigeon, J.; Le Liepvre, S.; Vassant, S.; Belabas, N.; Bardou, N.; Minot, C.; Yacomotti, A.; Levenson, A.; Charra, F.; Barbay, S. Strong Coupling between Self-Assembled Molecules and Surface Plasmon Polaritons. *J. Phys. Chem. Lett.* **2017**, *8* (22), 5626–5632.
(30) Sghaier, T.; Le Liepvre, S.; Fiorini, C.; Douillard, L.; Charra, F. Optical Absorption Signature of a Self-Assembled Dye Monolayer on Graphene. *Beilstein J. Nanotechnol.* **2016**, *7*, 862–868.
(31) Le Liepvre, S.; Du, P.; Kreher, D.; Mathevet, F.; Attias, A.-J.; Fiorini-Debuisschert, C.; Douillard, L.; Charra, F. Fluorescent Self-Assembled Molecular Monolayer on Graphene. *ACS Photonics* **2016**, *3* (12), 2291–2296.
(32) Vitukhnovsky, A. G.; Sluch, M. I.; Warren, J. G.; Petty, M. C. Observation of Perylene Excimers in Langmuir—Blodgett Films. *Chem. Phys. Lett.* **1991**, *184* (1–3), 235–238.
(33) Mahrt, J.; Willig, F.; Storck, W.; Weiss, D.; Kietzmann, R.; Schwarzburg, K.; Tufts, B.; Troesken, B. Luminescence and Configurations of Perylene Dimers in a Langmuir-Blodgett Film. *J. Phys. Chem.* **1994**, *98* (7), 1888–1894.

(34) Akimoto, S.; Ohmori, A.; Yamazaki, I. Dimer Formation and Excitation Relaxation of Perylene in Langmuir−Blodgett Films. *J. Phys. Chem. B* **1997**, *101* (19), 3753–3758.
(35) Antunes, P. A.; Constantino, C. J. L.; Aroca, R. F.; Duff, J. Langmuir and Langmuir−Blodgett Films of Perylene Tetracarboxylic Derivatives with Varying Alkyl Chain Length: Film Packing and Surface-Enhanced Fluorescence Studies. *Langmuir* **2001**, *17* (10), 2958–2964.
(36) Ma, K.; Wang, R.; Rao, Y.; Zhao, W.; Liu, S.; Jiao, T. Langmuir-Blodgett Films of Two Chiral Perylene Bisimide-Based Molecules: Aggregation and Supramolecular Chirality. *Colloids Surf. Physicochem. Eng. Asp.* **2020**, *591*, 124563.
(37) Oliveira, O. N.; Caseli, L.; Ariga, K. The Past and the Future of Langmuir and Langmuir–Blodgett Films. *Chem. Rev.* **2022**, *122* (6), 6459–6513.
(38) de Mello, J. C.; Wittmann, H. F.; Friend, R. H. An Improved Experimental Determination of External Photoluminescence Quantum Efficiency. *Adv. Mater.* **1997**, *9* (3), 230–232.
(39) El-Daly, S. A.; Fayed, T. A. Photochemistry of N, Ń-Ditridecyl-3,4:9,10-Perylenetetracarboxylic Diimide in Chloromethane Solvents. *J. Photochem. Photobiol. Chem.* **2000**, *137* (1), 15–19.
(40) Eggeling, C.; Widengren, J.; Rigler, R.; Seidel, C. A. M. Photobleaching of Fluorescent Dyes under Conditions Used for Single-Molecule Detection: Evidence of Two-Step Photolysis. *Anal. Chem.* **1998**, *70* (13), 2651–2659.
(41) Demchenko, A. P. Photobleaching of Organic Fluorophores: Quantitative Characterization, Mechanisms, Protection. *Methods Appl. Fluoresc.* **2020**, *8* (2), 022001.
(42) Lieb, M. A.; Zavislan, J. M.; Novotny, L. Single-Molecule Orientations Determined by Direct Emission Pattern Imaging. *J. Opt. Soc. Am. B* **2004**, *21* (6), 1210.
(43) Clark, A. E.; Qin, C.; Li, A. D. Q. Beyond Exciton Theory: A Time-Dependent DFT and Franck−Condon Study of Perylene Diimide and Its Chromophoric Dimer. *J. Am. Chem. Soc.* **2007**, *129* (24), 7586–7595.
(44) Liepvre, S. L.; Gouesmel, A.; Nguyen, K. N.; Bocheux, A.; Charra, F. Changes in Optical Properties of Conjugated Molecules and Polymers upon Adsorption onto Graphene. *Mol. Cryst. Liq. Cryst.* **2017**, *655* (1), 5–15.
(45) Yuan, L.; Huang, L. Exciton Dynamics and Annihilation in WS_2 2D Semiconductors. *Nanoscale* **2015**, *7* (16), 7402–7408.
(46) Ribierre, J. C.; Ruseckas, A.; Knights, K.; Staton, S. V.; Cumpstey, N.; Burn, P. L.; Samuel, I. D. W. Triplet Exciton Diffusion and Phosphorescence Quenching in Iridium(III)-Centered Dendrimers. *Phys. Rev. Lett.* **2008**, *100* (1), 017402.
(47) Ribierre, J. C.; Ruseckas, A.; Samuel, I. D. W.; Barcena, H. S.; Burn, P. L. Influence of the Dendron Chemical Structure on the Photophysical Properties of Bisfluorene-Cored Dendrimers. *J. Chem. Phys.* **2008**, *128* (20), 204703.
(48) Diggle, P. C.; Gehring, K. A.; Macfarlane, R. M. Exciton-Exciton Annihilation in TbPO4. *Solid State Commun.* **1976**, *18* (3), 391–394.